Low temperature magnetism of Ln_2Ba (Ln=Nd, Er, Ho) furoate-based polymeric chains: slow relaxation, magnetic anisotropy and interactions

Ana Arauzo,[a*] Elena Bartolomé,[b,c*] Javier Luzón,[a,d] Silvia Melnic,[e,f] Sergiu Shova[g] and Juan Bartolomé[a]

[a]Instituto de Nanociencia y Materiales de Aragón (INMA), CSIC-Universidad de Zaragoza, Pedro Cerbuna 12,50009 Zaragoza, Spain. E-mail: aarauzo@unizar.es

[b]Institut de Ciència de Materials de Barcelona (ICMAB), Bellaterra, Spain, E-mail: ebartolome@icmab.es

[c]Escola Universitària Salesiana de Sarrià (EUSS), Passeig Sant Joan Bosco 74, 08017-Barcelona, Spain. E-mail: ebartolome@euss.es

[d]Centro Universitario de la Defensa, Academia General Militar, Zaragoza, Spain

[e]Moldova State University, Institute of Chemistry, Academiei 3, MD-2028 Chisinau, Republic of Moldova

[f]"Nicolae Testemitanu" State University of Medicine and Pharmacy, bd. Stefan cel Mare şi Sfant 165, MD-2004 Chisinau, Republic of Moldova

[g]"Petru Poni" Institute of Macromolecular Chemistry, Alea Gr. Ghica Voda 41A, 700487 Iasi, Romania

(*) E-mail: aarauzo@unizar.es; ebartolome@icmab.es

Abstract

The synthesis, structure and magneto-thermal properties of three new lanthanide 1D polymeric complexes, $\{[Ln_2Ba(\alpha\text{-fur})_8(H_2O)_4]\}_n$ for Ln = Nd (**1**), Er (**2**) and $\{[Ho_2Ba(\alpha\text{-fur})_8(H_2O)_4]\cdot 2H_2O\}_n$ (**3**), based on carboxylic $\alpha\text{-fur} = C_4H_3OCOO$ ligands is reported. The α-furoate ligands consolidate zig-zag chains formed by Ln_2 dimers separated by Ba ions. *Ab initio* calculations, in combination with the fit of experimental static magnetization and heat capacity, predict the magnetic ground state, energy levels and magnetic interactions in these heteronuclear nanomagnets. Nd_2Ba (**1**) presents two different coordination sites for Nd, with an orthorhombic magnetic ground state. Nd ions are coupled along the chain through a weak antiferromagnetic (AF) interaction $J''/k_B = -0.08$ K. Er(III) ions in Er_2Ba (**2**) present a highly axial ground state, forming magnetic dimers with an interaction of $J'/k_B = -8.6$ K, while interdimer coupling along the chain is $J''/k_B = -0.28$ K. The Ho_2Ba (**3**) complex consists of a highly anisotropic quasi-doublet with a $\Delta_{Ho}/k_B = 0.7$ K gap. Non-Kramers Ho ions form magnetic dimers within the Ho_2Ba cluster, coupled by an AF intradimer interaction $J'/k_B = -2.5$ K. The three complexes exhibit in-field slow relaxation of the magnetization: **1** relaxes through an Orbach process at high temperatures ($U_{eff}/k_B=60(1)$ K) evolving to quantum tunneling below 3 K ($\tau_{QT}= 0.05(1)$ s); **2** exhibits a rapid Orbach-like process ($\tau_0= 8(6) \times 10^{-8}$ s and $U_{eff}/k_B=10(2)$ K) and **3** shows a direct process ($\tau = 0.4(1)$ s).

Keywords: single-molecule magnets, polymeric nanomagnets, slow magnetic relaxation

1. Introduction

Single-ion magnets (SIMs), single-molecule magnets (SMMs), and single-chain magnets (SCMs) are currently under intense research due to their intriguing physical properties, which encompass, magnetic hysteresis, slow relaxation and quantum tunneling of the magnetization.[1] Moreover, these materials hold promise for various applications such as high-density information storage, quantum computing,[2] quantum sensors, and molecular spintronics.

In particular, molecular magnets based on lanthanide (Ln) ions have garnered increasing attention in recent years.[3,4] In mononuclear SIMs, the slow-relaxation dynamics relies upon the formation of an energy barrier (U_{eff}) between two stable energy states, which is primarily influenced by the molecule's anisotropy,[5] determined by the type of lanthanide and its coordination environment, including factors as its symmetry,[6] the number and type of coordinating atoms, as well as ligands in the first and even the second coordination sphere.[7] Extremely large activation energies at record blocking temperatures have recently been reported for certain Dy metallocenes thanks to the rigid, axial geometry achieved by the ligands, $[Dy(Cp^{ttt})_2]$ (U_{eff}=1760 K at T_B=60 K)[8] and $[(Cp^{iPr5})Dy(Cp^*)]^+$ (U_{eff}=2217.2K at T_B=80 K)[9]. This latter result paves the way for the development of nanomagnetic devices operating at practical, liquid-nitrogen temperatures.

Dinuclear [Ln$_2$] compounds have attracted interest for various reasons. Ln$_2$ complexes such as Tb$_2$Pc$_3$ (double-decker phthalocyanines) have been intensively investigated due to their tendency toward high energetic barriers and their potential of customization onto surfaces.[10] In specific cases, it has been noted that weak inter- and intramolecular interactions can serve as a bias molecular field reducing quantum tunneling relaxation.[11] Additionally, weakly-coupled asymmetric [LnLn'] compounds have been suggested as candidates for realizing quantum gates performing CNOT and SWAP operations between two coupled two-level bits (qubits),[12] or implementing multi-level quantum bits (qudits).[13]

On the other hand, lanthanide-based 1D polymeric compounds are appealing for the preparation of low dimensional, multifunctional magnetic systems.[14] Moreover, they represent ideal models for investigating magnetic relaxation as a function of the type of ion, anisotropy and relative strength of intra-chain and inter-chain interactions. The slow relaxation of the magnetization phenomenology can range from SIM behavior in 1D systems coordinating magnetically isolated ions, to SCM behavior governed by Glauber dynamics in chains containing strongly ferromagnetically coupled Ising spins.[15] Polymeric chains based on a variety of ligands have been reported, including azido,[16] dithienylethene,[17] anthraquinone,[18] and cyanoacetate ligands.[19]

In our previous research, we reported the successful utilization of the α-furoate ligand in a bridging mode to create 1D polymeric chains of lanthanides. This approach enabled the synthesis of homonuclear $\{Ln(\alpha\text{-fur})_3(H_2O)_3\}_n$ complexes, featuring either Kramers (Dy,[20] Nd[21]) or non-Kramers (Tb[22]) ions, as well as a heteronuclear complex (Ln=Tb/Eu),[23] and dinuclear complexes $\{[Ln_2Ba(\alpha\text{-fur})_8(H_2O)_4]\cdot 2H_2O\}_n$ (Ln=Dy[24], Tb[25]), to investigate the dynamic behavior as a function of the character of the magnetic Ln, and Ln-Ln interactions. In recent years, our research group has employed a multi-technique characterization of these polymeric Ln-furoate complexes, extending down to millikelvin (mK) temperatures, to scrutinize the relaxational behavior as both intrachain and interchain interactions progressively become competitive. The results have revealed a plethora of relaxational behaviors, ranging from SIM behavior of isolated ions in two different coordination sites in the Dy compound,[20] to SCM behavior enabled by the presence of defects in antiferromagnetic (AF) Tb chains,[22]. Additionally, slow relaxation was observed in Dy_2Ba ferromagnetic chains undergoing a transition to 3D order at very low temperatures,[24] while Tb_2Ba in Ising AF transverse displayed a sluggish magnetic relaxation.[25]

The Ln_2Ba members of this family are composed by a dimeric magnetic unit separated by an alkaline earth (AE). AE metals exhibit versatile coordination numbers and potential linkage capabilities.[26,27] Heterometallic coordination compounds formed by lanthanide and alkaline earth metals of diverse dimensionalities have been reported, including trinuclear clusters,[28] 1D coordination polymers,[26,29] among which ladder shaped chains,[30] 2D structures[29,31] and 3D frameworks.[27] However, previous investigations of 1D AE-Ln-CPs have primarily focused on the luminescent properties of the compounds, with magnetic comprehension notably lacking.

Herein, to complete our systematic investigation of 1D α-furoate polymers, we report the synthesis and magneto-structural characterization of three novel heterometallic compounds, namely $\{[Nd_2Ba(\alpha\text{-fur})_8(H_2O)_4]\}_n$, **(1)** Nd_2Ba, and $\{[Er_2Ba(\alpha\text{-fur})_8(H_2O)_4]\}_n$, **(2)** Er_2Ba, (featuring Kramers ions), and $\{[Ho_2Ba(\alpha\text{-fur})_8(H_2O)_4]\cdot 2H_2O\}_n$, **(3)** ($Ho_2Ba$) featuring the non-Kramers Ho ion. They consist of trinuclear clusters (Ln-Ba-Ln) (Ln= Nd, Er, Ho), linked by furoic bridges, forming zig-zag chains.

This work provides physical insight into the crystal structure, static, and dynamic magnetic properties of the three new complexes **1**, **2**, and **3**. These findings are discussed in the context of *ab initio* calculations of the energy level distribution. Additionally, the relaxational phenomenology of these new complexes is compared with the previously reported α-furoate Ln compounds.

2. Materials and Methods

a. Synthesis

The complexes $\{[Ln_2Ba(\alpha\text{-}fur)_8(H_2O)_4]\}_n$, where Ln = Nd (**1**), Er (**2**) and $\{[Ho_2Ba(\alpha\text{-}fur)_8(H_2O)_4]\cdot 2H_2O\}_n$ (**3**), represent examples of carboxylate mixed-metal 1D polymers. These clusters were synthesized in a single step starting from $Ba(\alpha\text{-}fur)_2\cdot 4H_2O$, where α-fur is α-furancarboxylic acid, and $Ln(ClO_4)_3\cdot 6H_2O$. The complete synthetic procedure is detailed in reference,[32] outlining the optimized conditions for the preparation of 1D polymer structures. The synthesis involved mixing $Ba(\alpha\text{-}fur)_2\cdot 4H_2O$ (0.70 mmol) in 5 ml of water with $Ln(ClO_4)_3\cdot 6H_2O$ (0.70 mmol) in 10 ml of ethanol at room temperature, resulting in the formation of a lilac (1) (slightly pink (2) or white (3)) gel-mass. Subsequently, 10 ml of water were added to the obtained compound, which was stirred for an additional period of 20-30 minutes at 50 °C to yield a clear solution. Allowing the solution to stand for a week led to the precipitation of microcrystalline material, which was then filtered off, washed with water, and air-dried. The FT-IR spectra of the samples confirmed the presence of characteristic bands. A broad absorption band at 3500-3300 cm^{-1} appeared due to the stretching frequency $\nu(O–H)$ of the coordinated H_2O. Typical COO stretching modes were observed at 1627-1628 cm^{-1} and 1586-1588 cm^{-1}. Additional features in the FT-IR spectra for 1-3 included absorption bands in the 883–884 cm^{-1} regions attributed to a five-membered aromatic furan ring. Elemental analyses of the complexes were consistent with their molecular formulas.

b. Experimental methods

The magnetization, dc and ac susceptibility of powdered samples were measured, above 1.8 K, using a Quantum Design superconducting quantum interference device (SQUID) magnetometer. Data were corrected from all diamagnetic contributions from the capsule and oil used in sample preparation. Ac measurements were conducted at an excitation field of 4 Oe, and under dc fields between 0-30 kOe, while sweeping the frequency between 0.1 and 1000 Hz. Additionally, ac measurements in an extended

frequency range, 90< f< 10000 Hz, were carried out using a Quantum Design PPMS ACMS susceptometer. Measurements on powdered samples were done with the addition of Daphne oil, introduced to immobilize the grains at low temperatures.

Low temperature heat capacity under various applied fields (0-30 kOe) was measured on a powder-pressed pellet fixed with Apiezon N grease. The measurements were conducted using the same PPMS, equipped with a [3]He refrigerator.

c. Simulation methods

Relativistic *ab initio* calculations were performed using the CASSCF/RASSI-SO35 method as implemented in the MOLCAS 8.6 package.[33] This relativistic quantum-chemistry approach has proven suitable to analyse the magnetic anisotropy and direction of the easy axis of magnetization (EAM) of lanthanide ions.[34] The atomic positions were extracted from the x-ray crystal structure. The cluster model for the three complexes **1-3** includes the studied Ln(III) ion, its ligands, 6 furoate molecules and two waters. It also includes the closest Ln(III) ion, replaced by a La(III) in order to reduce the active space, the two closest Ba(II) ions and a simplified version of their ligands (see Fig. S1 in SI).

For the three complexes, all atoms were represented by basis sets of atomic natural orbitals from the ANO RCC library: the VQZP basis-set for the Ln ions, the VTZP one for the O, C and H atoms in the first, second and third shells around the Ln ion, and the VDZ one for all the other atoms.

Finally, the chosen CASSCF active space consisted of the Ln 4f orbitals, containing 3, 10 and 11 electrons for, respectively, the Nd, Er and Ho ions. (CASSCF(3,7), CASSCF(10,7) and CASSCF(11,7)). The RASSI-SO steps were performed on averaged-state CASSCF calculations including all quadruplets for the Nd and the Ho derivatives and all the quintuplets for the Er derivative (35 roots for each of the three complexes).

3. Structural characterization

The crystals of the isolated complexes **1-3** were of suitable quality to collect X-ray diffraction data and to solve the structures. Single-crystal X-ray diffraction data for **2** and **3** were collected on an Oxford-Diffraction XCALIBUR Eos CCD diffractometer with graphite-monochromated Mo Kα radiation. The unit cell determination and data

integration were carried out using the CrysAlisPro package from Oxford Diffraction.[35] Multi-scan correction for absorption was applied. The structure was solved with SHELXT program using the intrinsic phasing method and refined by the full-matrix least-squares method on F^2 with SHELXL.[36, 37] Olex2 was used as an interface to the SHELX programs.[38] Non-hydrogen atoms were refined anisotropically. Hydrogen atoms attached to carbon atoms were added in idealized positions and refined using a riding model. Selected crystallographic data and structure refinement details for **2** and **3** are provided in Table 1 and the corresponding CIF-files. The main crystallographic data and refinement details for **1** can be found in reference [32]. The supplementary crystallographic data can be obtained free of charge via www.ccdc.cam.ac.uk/conts/retrieving.html (or from the Cambridge Crystallographic Data Centre, 12 Union Road, Cambridge CB2 1EZ, UK; fax: (+44) 1223–336-033; or deposit@ccdc.ca.ac.uk) Figure 1 illustrates the structures of compounds **1**, **2**, and **3**.

Table 1. *Crystal data and details of structure refinement for **2** and **3**.*

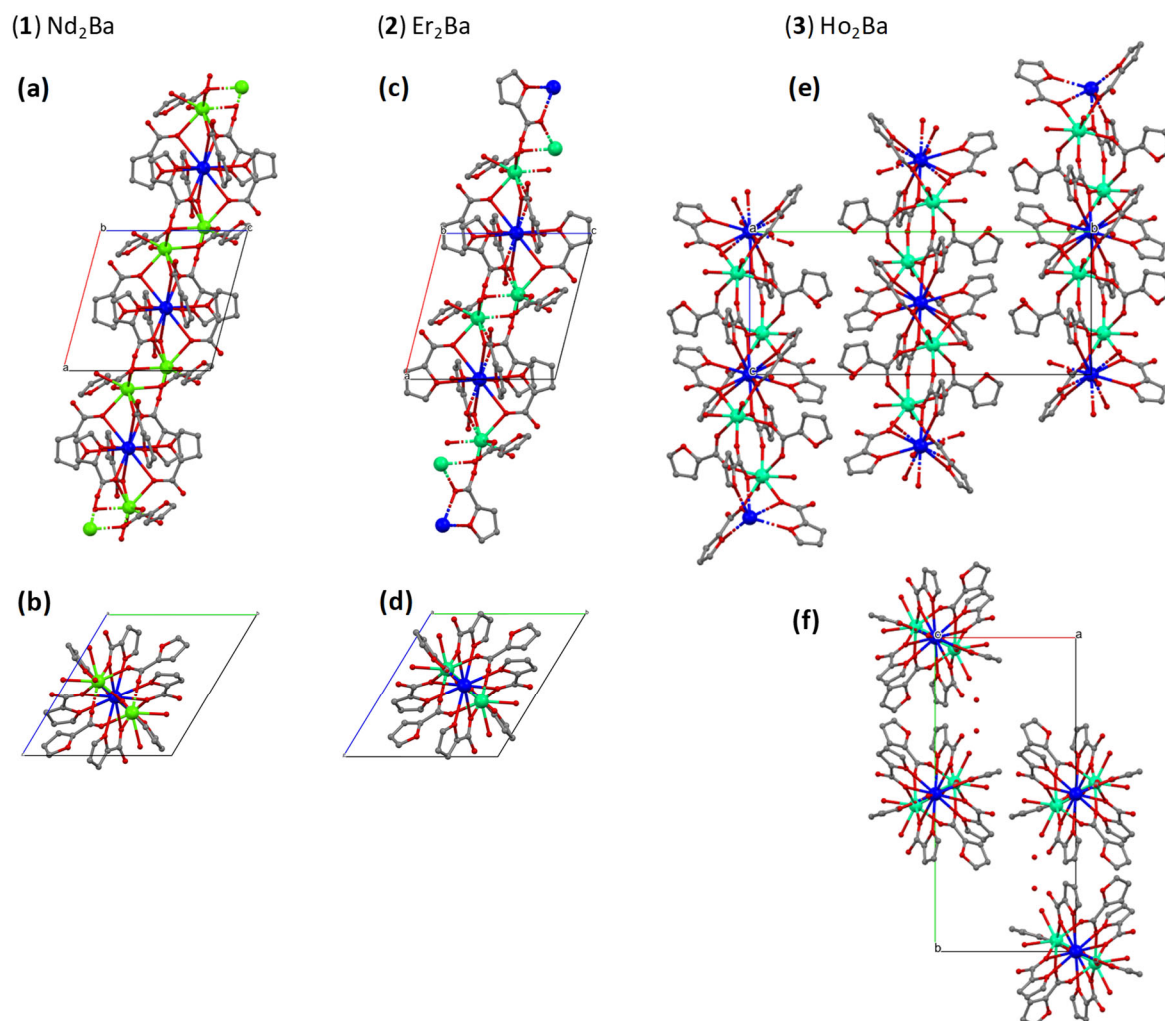|	2	3
Emp. formula	$C_{40}H_{32}BaEr_2O_{28}$	$C_{40}H_{36}BaHo_2O_{30}$
Fw	1432.51	1463.89
T [K]	160.00(10)	293
space group	$P\text{-}1$	$P2_1/c$
a [Å]	10.5646(4)	11.2985(11)
b [Å]	11.0761(9)	22.706(2)
c [Å]	11.4488(8)	10.5477(11)
α [°]	118.434(8)	90
β [°]	93.126(4)	115.811(12)
γ [°]	108.451(5)	90
V [Å^3]	1083.16(14)	2436.0(5)
Z	1	2
ρ_{calcd} [g cm^{-3}]	2.196	1.996
μ [mm^{-1}]	4.841	4.114
Crystal size [mm]	0.45 × 0.05 × 0.05	0.80 × 0.20 × 0.20
2Θ range	4.174 to 50.044	4.004 to 48.812
Refls. collected	6761	14231
Indep. Refls., R_{int}	3799, 0.0352	3979, 0.0615
Data/rests./params.	3799/0/322	3979/0/331
GOF	1.045	1.115
R_1, wR_2(all data)	0.0343, 0.0795	0.0452, 0.0966
CCDC no.	2315669	2315668

Figure 1. *Crystal structure of α-furoate based Ln₂Ba polymeric compounds: (1) Nd₂Ba: (a) view along b-axis and (b) a-axis; (2) Er₂Ba: (c) view along b-axis and (d) a-axis; (3) Ho₂Ba: view along a-axis (e) and (f) c-axis. Color code: Ln (green), Ba (blue), O (red), C (grey), H atoms have been omitted for clarity.*

Crystal structure of {[Nd₂Ba(α-fur)₈(H₂O)₄]}ₙ (1)

The complex **1** crystallises in the triclinic space group P-1. Its crystal structure is described in reference[39] and depicted in Figure 1a.

Crystal structure of {[Er₂Ba(α-fur)₈(H₂O)₄]}ₙ (2)

The complex **2** crystallises in the triclinic space group P-1, and the molecular structure exhibits one-dimensional (1D) coordination polymer isostructural to compound **1**. In the crystal the erbium atom occupies a general position, while Ba atoms reside at the

special position - the center of inversion. Such an arrangement ensures the formation of a zig-zag metal chain along the *a*-direction in the crystal (Figure 1b and 2a), $\cdots Er \cdots Er \cdots Ba \cdots Er \cdots Er \cdots$.

Crystal structure of $\{[Ho_2Ba(\alpha\text{-fur})_8(H_2O)_4]\cdot 2H_2O\}_n$ (3)

The single-crystal X-ray diffraction (XRD) study reveals that complex (**3**) crystallizes in the space group P21/c of the monoclinic system, and is isostructural to $\{[Tb_2Ba(\alpha\text{-fur})_8(H_2O)_4]\cdot 2H_2O\}_n$[25] and $\{[Dy_2Ba(\alpha\text{-fur})_8(H_2O)_4]\cdot 2H_2O\}_n$[24] compounds. Complex **3** is comprised of Ho–Ba–Ho clusters linked end-to-end. Within each cluster, the Ho^{3+} and Ba^{2+} ions, as well as the Ho^{3+}–Ho^{3+} ions of adjacent clusters, are connected through the bridging function of polydentate furoic acid ligands, forming a 1D zig-zag coordination polymer along the *c*-direction, as illustrated in Figure 1c and 2b.
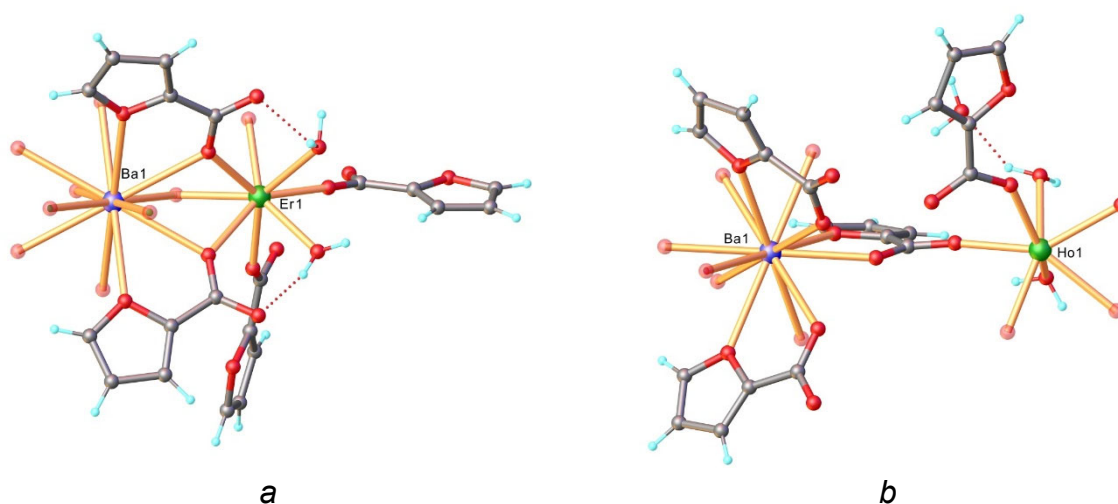

a	*b*

Figure 2. *View of the asymmetric unit with selected atom labelling in the crystal structure of **2** and **3**. Symmetry generated atoms are shown with faded colours.*

4. Static magneto-thermal properties

The static magnetic properties of compounds **1**, **2** and **3** were characterized by measuring the field dependence of the magnetization $M(H)$ at 1.8 K, and the equilibrium dc susceptibility as a function of the temperature at 1 kOe from 1.8 K to 300 K (refer to Figure 3). Thermal properties were characterized my measuring the specific heat as a function of temperature, $C_P(T)$, at different applied magnetic fields (Figure 4).

Nd₂Ba (1)

Nd(III) is a Kramers ion with a free ion $^4I_{9/2}$ ground state (S=3/2, L=6, J=9/2, g_J=8/11), which is split by the ligand field into five Kramers doublets, with the lowest doublet being the only one populated at very low temperatures on the order of a few Kelvin. The obtained room temperature value per Nd(III) ion is χT(300 K) = 1.52 emu.K/mol (see Fig. 3a). The fit of the χ^{-1} curve to a Curie-Weiss law above 150 K, yields a Curie constant of C = 1.53 emuK/mol per Nd(III) ion which corresponds to an effective moment μ_{eff} = 3.61(1) μ_B, in fully agreement with the expected value for the value for a free Nd(III) ion, μ_{eff} = 3.62 μ_B. The obtained Curie temperature is negative and rather large, θ = -21.1±0.6 K, indicative of overall antiferromagnetic (AF) interactions in this complex. χT decreases as the temperature is reduced, as a result of the thermal depopulation of the excited doublets, and reaches 0.56 emu.K/mol at 1.8 K.

XRD characterization of **1** reveals two slightly different sites for Nd(III) in the dimer. The inversion symmetry is broken and causes a dissymmetry in the two Nd(III) ions forming the Nd₂Ba cluster. This effect of lowering of the symmetry in this complex allows the formation of a magnetic dimer hosting two different centers, well separated by the Ba cation, disposed in 1D polymeric chains, which makes this complex of additional interest for quantum processing.[40] Each Nd(III) center has its own energy levels and magnetic anisotropy. A small magnetic interaction gives rise to a manyfold of energy levels for quantum operations.

Ab initio calculations of the energies of the excited doublets have been performed for the two different Nd sites, yielding the five Kramers doublets at the energies 0, 117.4, 237.7, 315.7, 405.5 K for Nd1, and 0, 99.7, 252.1, 318.9, 394.1 K for Nd2. The easy axis of magnetization (EAM) for each of the Nd ions in the dimer, depicted in Fig. 5a, does not coincide with any of the site symmetry axes of the crystal. The ground state doublet for each Nd is expressed in effective spin S^* = 1/2, with g^* factors: g^*_x = 0.79, g^*_y = 1.14, g^*_z = 4.36, for Nd1 and g^*_x = 1.07, g^*_y = 1.79, g^*_z = 3.91, for Nd2 where z is the principal axis of the g^* tensor. It does not correspond to any principal crystallographic axis. Therefore, though the predominant anisotropy is along the z-axis, the transversal component is significant.

The Hamiltonian describing the quantum behavior of the system at low temperatures can be written in terms of the S^* = 1/2 effective spin, with a term for

Zeeman interaction and a term including the magnetic interaction along the chain within the Ising exchange interaction model:

$$\mathcal{H} = \mathcal{H}_z + \mathcal{H}_{ex} = \sum_i \mu_B \left(g_{i,x}^* S_{i,x}^* H_x + g_{i,y}^* S_{i,y}^* H_y + g_{i,z}^* S_{i,z}^* H_z \right) - 2 \sum_i J^*(i, i+1) S_{z,i}^* S_{z,i+1}^* \quad (1)$$

with $J^*(i, i+1) = J'$ and J'' for $i=$ even and odd, respectively. Inter-chain interactions, J''', are neglected in this model. In the instance where $J'' = 0$, the Hamiltonian simplifies to that of a magnetic dimer case. In the analysis below for Nd$_2$Ba, we have considered the case where interdimer and intradimer interactions are comparable, denoted as $J' = J''$.

The field-dependence of the magnetization measured at $T=1.8$ K is shown in Fig. 3b. The $M(H)$ data is compared with the simulated curve derived from Eq. 1 assuming J'' =0 (dimer model). A linear Van Vleck term is added to account for the effect of excited levels. The experimental data falls below the calculated curve for a non-interacting dimer, pointing to the existence of overall AF interactions. While the magnetization matches the simulation for a Nd1Nd2 dimer with $J'/k_B = -0.4$ K, this model would yield a broad maximum in the $C_P(T)$ at zero field around 0.3 K, which is not observed (see below). Consequently, we can establish an upper limit for the dimer interaction to be significantly below -0.4 K. The lower $M(H)$ values are attributed to the influence of overall AF interactions along the chain.

Fig. 4a shows the heat capacity as a function of temperature measured at different fields. The heat capacity at zero field has been modeled as the sum of two contributions,

$$C_P = C_m + C_{lat} = \frac{R}{T^2} \left[\frac{(J'/2k_B)^2}{cosh^2(J'/2k_B T)} \right] + AT^3. \quad (2)$$

The lattice contribution dominating the heat capacity above 2 K was fitted by the Debye approximation, $C_{lat} = AT^3$, with A/R = 1.62±0.01 × 10^{-3}K^{-3}, from which a Debye temperature of $\theta_D = 250\pm2$ K was obtained. Below 2 K, we observed a high temperature tail with a T^{-2} power law. We have modeled this magnetic contribution with a $S^* = 1/2$

Ising chain (see Eq. 1 and 2), which yields a value for the average Nd-Nd intrachain exchange interaction of $|J'| = |J''| \approx 0.08$ K.

At $H \neq 0$, clear Schottky type anomalies show up. The experimental curves are typical of the heat capacity of a two-level system with increasing energy splitting. They have been simulated with program PHI[41] to the predicted C_P for a magnetic field split Kramers doublet due to Zeeman interaction with *ab initio* obtained g^* values (Fig. 4b). This analysis takes into consideration only the Zeeman term in Eq. 1, neglecting in a first approximation the effect of the magnetic interaction observed at lower temperatures. As shown in Fig. 4b, the calculated curves reproduce well the experimental data measured for H = 5 to 30 kOe.

Er₂Ba (2)

Er(III) is also a Kramers ion, characterized by a free ion $^4I_{15/2}$ ground state (S=3/2, L=6, J=15/2, g_J=6/5). The ligand crystal field further splits this state into eight Kramers doublets, with only the lowest doublet being populated at low temperatures. The measured room temperature value per Er(III) ion is χT(300 K)= 11.0 emu.K/mol (see Fig. 3c). From the fit of the χ^{-1} curve to a Curie-Weiss law above 100 K, we obtain a Curie constant of C = 11.22±0.01 emuK/mol per Er (III) ion, yielding an effective moment μ_{eff}= 9.48(1) μ_B very close to the expected value for a free Er(III) ion, μ_{eff} = 9.58 μ_B. The obtained Curie temperature is negative, θ = -4.9±0.1 K, indicative of overall AF interactions in **2**. χT decreases as the temperature is reduced, as a result of the thermal depopulation of the excited doublets, and reaches 5.35 emu.K/mol at 1.8 K.

Ab initio calculations were conducted to obtain the energies of the eight Kramers doublets for Er(III), located at 0, 88.9, 97.4, 160.7, 227.1, 274.2, 351.3, 385.0 K, and the EAM of the two Er ions in the dimer, depicted in Fig. 5b. The ground state doublet for Er shows a high axiality and can be expressed in effective spin S^* = 1/2, with g^* factors: g^*_x = 0.01, g^*_y = 0.02, g^*_z = 17.54.

The $M(H)$ data at 1.8 K is presented in Fig. 3d, and compared with the simulated curve derived from Eq. 1 utilizing *ab initio* obtained g^* values for the ground doublet. The experimental data falls significantly below the simulated curve for a non-interacting dimer, evidencing the presence of strong AF interactions in this system. A pure dimer

model fails to reproduce the observed behaviour, pointing towards a more intricate AF interacting scenario, which can be further disclosed by examining the low T heat capacity data.

Indeed, $C_P(T)$ obtained at zero magnetic field (Fig 4c) exhibits several relevant features. Apart from the lattice contribution in the high temperature region, we observe a soft bump centered at 4 K of magnetic origin, caused by some splitting of the Er dimer levels. It has been modeled with program PHI using the g^* values obtained by *ab initio* and a large intradimer interaction of $|J'|/k_B = 8.6$ K. The increase of $C_P(T)$ below 1 K is attributed to intrachain interdimer magnetic interactions, $C_m/R = A_{ex}T^{-2}$ ($A_{ex} = 4.5\pm0.2\ 10^{-2}$ K^2), that can be modelled with Eq. 2 for a $S^*=1/2$ Ising chain, given the highly anisotropic character of the Er(III) in the ground state (Fig. 4d). We obtain an average value for the exchange interaction of $|J''| = 0.28$ K. The variation of $C_P(T)$ with the magnetic field cannot be reproduced with a pure dimer model, as the intradimer interactions are too significant to be neglected.

Ho$_2$Ba (3)

Ho(III) is a non-Kramers ion with a free ion ground state of $^5I_8$ ($S=2$, $L=6$, $J=8$, $g_J=5/4$). At very low temperatures, typically only a ground state pseudo-doublet is thermally populated.

The observed room temperature value per Ho(III) ion is $\chi T(300$ K$) = 13.3$ emu.K/mol (see Fig. 3e). The fit of the χ^{-1} curve to a Curie-Weiss law above 100 K, yields a Curie constant of $C = 13.53 \pm 0.01$ emuK/mol per Ho (III) ion, which corresponds to an effective moment $\mu_{eff}= 10.40(1)\ \mu_B$ very close to the expected value for a free Ho(III) ion $\mu_{eff} = 10.6\ \mu_B$. The obtained Curie temperature is negative, $\theta = -4.9\pm0.3$ K, indicative of overall AF interactions in **3**. χT decreases as the temperature is reduced, as a result of the thermal depopulation of the excited levels, and reaches 5.85 emu.K/mol at 1.8 K.

Ab initio calculations yields the energies of the 2J+1 levels, which are closely packed in pseudo-doublets, 0, 0.77, 58.65, 59.24, 105.89, 112.73, 181.14, 185.82, 189.12, 214.56, 277.73, 296.79, 304.13, 327.61, 341.00, 384.18 and 384.74 K. The EAM for the Ho ions in the dimer is depicted in Fig. 5c. The ground state pseudo-doublet for Ho

is highly anisotropic, and can be expressed in effective spin $S^* = 1/2$, with g^* factors: $g^*_x = g^*_y = 0.0$, $g^*_z = 18.07$.

Similar to Er$_2$Ba, the isothermal magnetization at 1.8 K for Ho$_2$Ba is influenced by AF interactions (see Fig. 3f), which cannot be adequately accounted for solely by an AF dimer model. This suggests the presence of competitive dimer and interdimer intrachain interactions.

The heat capacity under H=0 for **3** at low temperatures, Fig. 4e, shows a lattice contribution dominant at temperatures above 5 K and a broad Schottky-like contribution of magnetic origin centered around 1 K. This broad maximum can be attributed to the non-Kramers splitting of the ground state pseudo-doublet, $\Delta_{Ho} = 0.7$ K, as obtained by *ab initio*, plus a magnetic interaction at dimer level of $|J'|/k_B$ =2.5 K (Fig. 4f). The upturn at low temperatures, dominant for a magnetic field of 5 kOe and above can be ascribed to the hyperfine splitting which is considerable large in the case of Holmium. Indeed, hyperfine interactions arising from ^{165}Ho (I=7/2) with a natural abundance of 100 % represent the predominant contribution to the specific heat below 1 K. Large hyperfine interaction between the electronic and nuclear spins of Ho commonly leads to a nuclear Schottky anomaly with a maximum at $\approx$0.3 K.[42] . Holmium has an hyperfine coupling parameter $A = 0.5$ K[43], which for I=7/2, gives a contribution $C_{hf}T^2/R = A^2 I(I+1)/12k_B^2 = 0.33$. In this complex, the high temperature tail is approximately $C_{hf}/R = 0.30(5)T^{-1.5}$ well within expected values although with a temperature dependence not exactly T^{-2}. Interestingly the hyperfine contribution is not present at zero magnetic field, which may be caused by a quench of the hyperfine coupling due to the dimer AF interaction, overcome in the presence of a polarizing magnetic field.
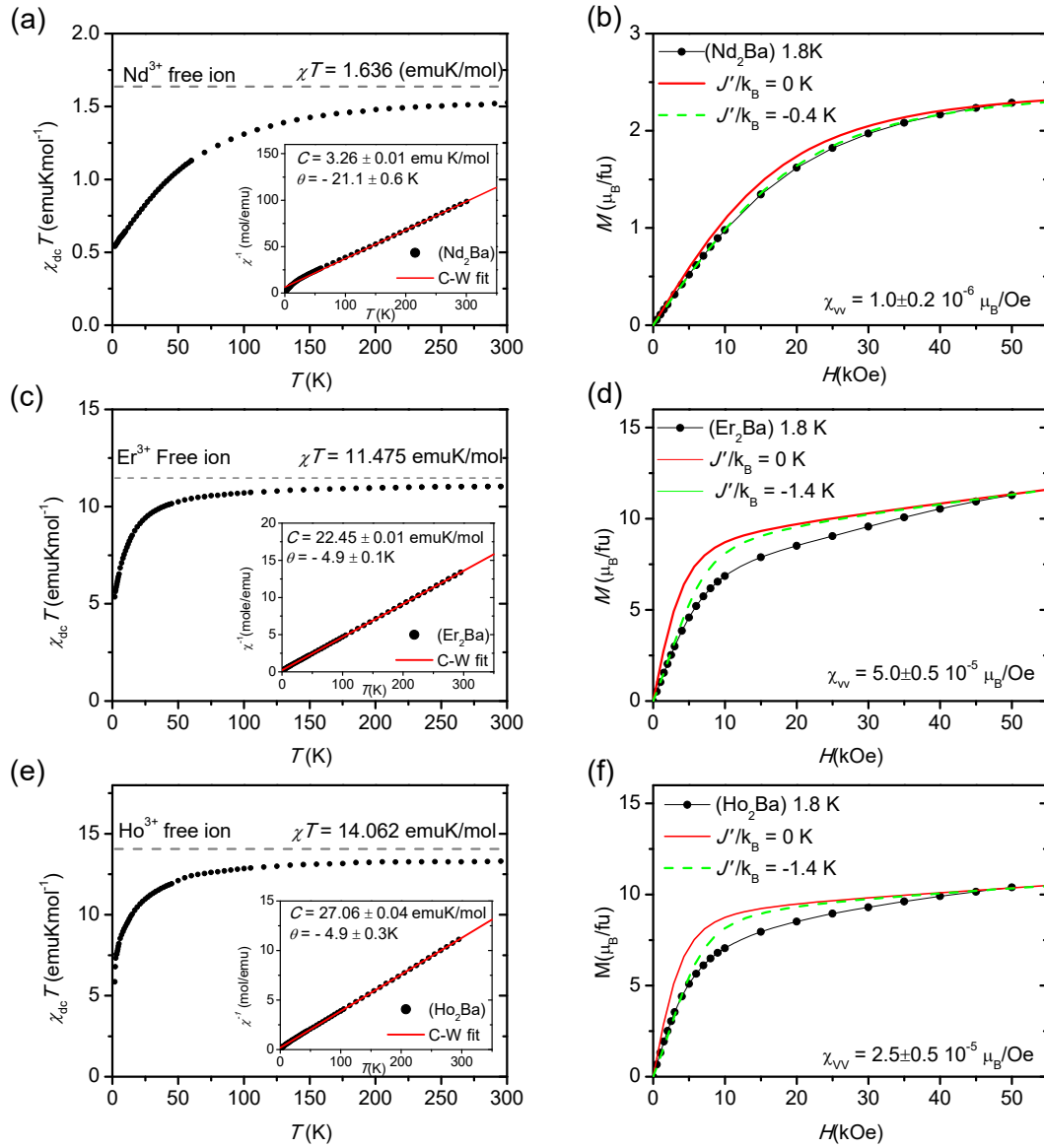
Figure 3. *Dc magnetometric characterization for **1, 2** and **3**. (Left) Temperature variation of the susceptibility-temperature product, per Ln(III) ion, (χT); Insert: Inverse of the magnetic susceptibility as a function of temperature, and fit to a Curie-Weiss law (solid red line), and (Right) Field-dependence of the isothermal magnetization, M(H), at T=1.8 K, for (**1**) Nd₂Ba (top), (**2**) Er₂Ba (middle), and (**3**) Ho₂Ba (bottom) compared with simulations within a dimer model (Eq. 1 for J''/k_B = 0). Case of non-interacting ions, i.e. no intradimer coupling, J'/k_B = 0 (solid red line) and AF dimers J'/k_B < 0 (green dashed line).*
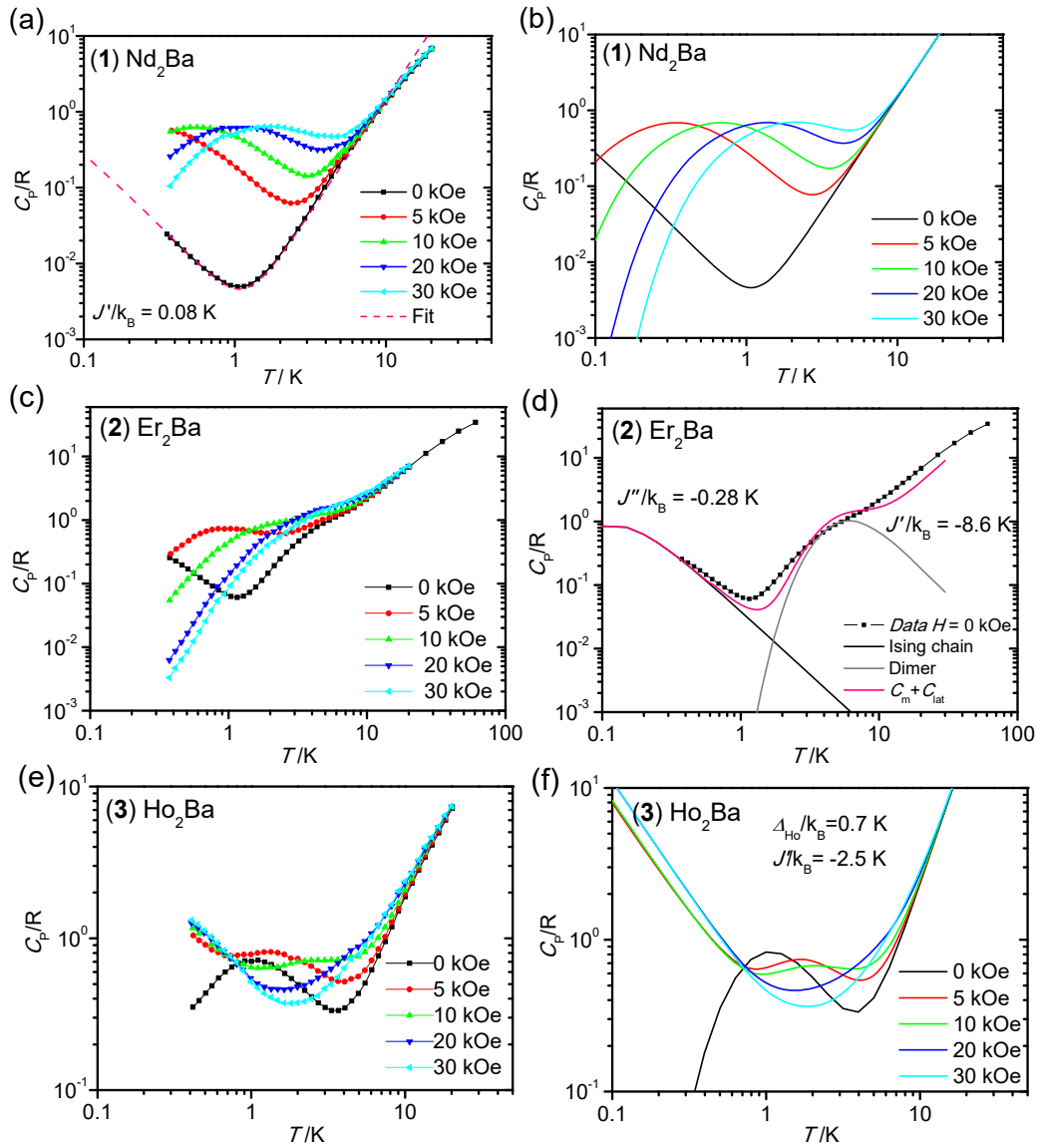
Figure 4. *Specific heat characterization for* **1**, **2** *and* **3**. *(Left) Experimental $C_P(T)$ at different magnetic fields H = 0, 5, 10, 20 and 30 kOe along with fit for complex* **1** *at H=0 according to Eq. 2 (A_L=1.62±0.01 10^{-3} R/K^3 and J'/k_B =J''/k_B = -0.08 K). (Right) Simulated $C_P(T,H)$ curves with magnetic contribution according to Eq. 1. Non-interacting dimers for* **1** *(b); Ising chain J'/k_B =J''/k_B = -0.28 K (Eq. 2) and AF dimer J'/k_B = -8.6 K for* **2** *(d); Hyperfine splitting, and AF dimer J'/k_B = -2.5 K for* **3** *(f).*
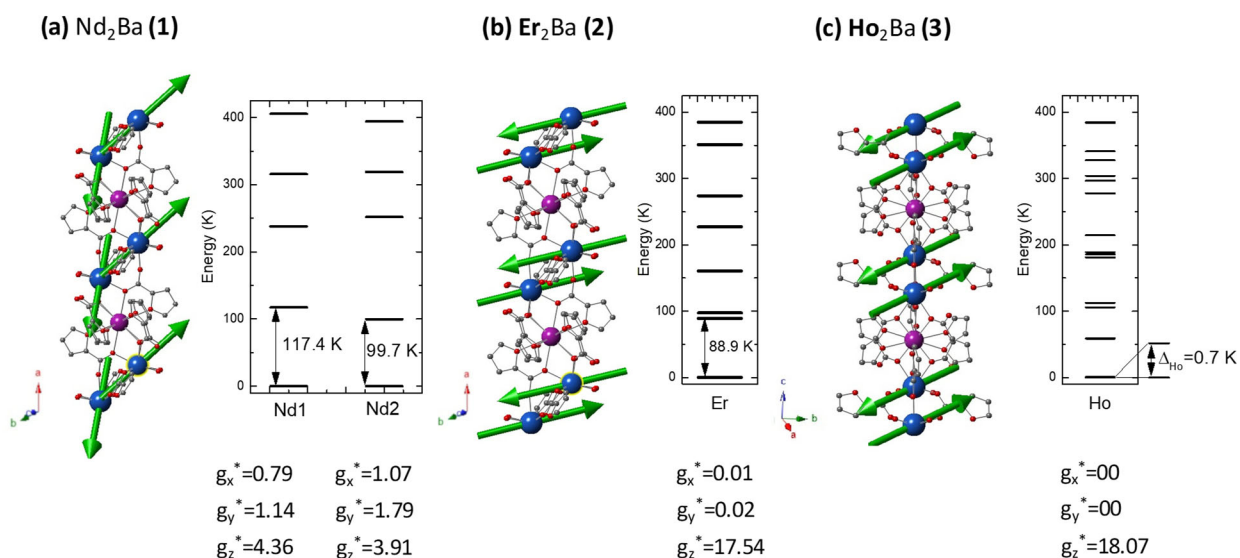
Figure 5. *Ln₂Ba coordination environment, ab initio calculated direction of the EAM, gyromagnetic values and energy levels of Ln ions in complexes 1, 2 and 3. Color code: Ln (blue), Ba (purple), O (red), C (grey), H atoms have been omitted for clarity.*

5. Dynamic properties

Ac susceptibility measurements at varying frequency, as a function of temperature and magnetic field, were performed to study the spin relaxation phenomena in **1**, **2** and **3**.

For the three complexes, at $H=0$, no contribution to the out-of-phase susceptibility, χ'', could be observed above 1.8 K, implying that there exists a relaxation process, related to quantum tunneling of the magnetization (QTM) with $\tau_{QT}<10^{-5}$ s faster than the frequency window of our experiment ($0.01<f<10$ kHz).

In the Kramers (Nd₂Ba) and (Er₂Ba) complexes, QTM would be in principle forbidden, however, it can be enabled by the existence of a non-zero effective field due to magnetic interactions that splits the Kramers degeneracy, and/or by the transverse components of the g^* tensor, which are important for the Nd(III) centers. In the case of Ho₂Ba, the ground state pseudo-doublet does not have any restriction for the spin relaxation via QTM. The application of an external magnetic field $H\neq0$ detunes the QTM process in all of them, allowing the observation of slow relaxation dynamics. The variation of the relaxation time with temperature and field discloses the different relaxation mechanisms taking place in these complexes.

Nd₂Ba (1)

The application of a relatively small magnetic field, even as low as 100 Oe, is sufficient to partially quench QTM, thereby allowing the observation of slow relaxation of the magnetization (see Fig. 6a,b). The variation of the relaxation time with the dc magnetic field H at 2 K remains nearly flat across most of the measured range, indicating a dominant relaxation mechanism via QTM at very low temperatures. No evidence of relaxation through a direct process is observed. An optimal field of 2 kOe has been applied, where nearly all the centers exhibit slow relaxation with a single relaxation time. Both, in-phase (χ') (see Fig S2 in SI) and out-of-phase (χ'') (Fig 6a) magnetic susceptibility curves exhibit a frequency dependence typical of process following the Debye model. A very low adiabatic contribution results in χ' approaching zero at high frequencies (see Fig S2 in SI). The obtained values of the relaxation time, $\tau(1/T)$, can be fitted with the following contributions:

$$\tau^{-1} = \tau_{QT}^{-1} + CT^n + \tau_0^{-1}\exp(-U_{eff}/k_BT),\qquad(3)$$

where the first term represents the relaxation via QTM, dominant at low temperatures, the second accounts for Raman relaxation, and the last for Orbach relaxation, dominant above 4 K.[43] A value for the τ_{QT}= 0.05(1) s is found, in agreement with the values observed in the $\tau(H)$ at 2 K (see Fig 6g, h). The determined Orbach activation energy, U_{eff}/k_B=60(1) K lower than first excited Kramers doublet energy obtained in *ab initio* calculations (117.4 K and 89.6 K for Nd1 and Nd2 respectively), with a prefactor τ_0= 3.5(5) x 10⁻⁹ s. Contribution to the relaxation due to Raman processes, amounts 0.183(4) T^6 s⁻¹. All of these values fall within the typical range reported for Nd ions.[21] The observed relaxation behavior is similar to that found in the previously studied monomeric Nd(α-fur) complex.[21] In both cases, the exchange interaction is very weak and of AF character, and dimeric formation in Nd₂Ba does not play a significant role in relaxation dynamics.

Er₂Ba (2)

At zero magnetic field, no slow spin relaxation is observed. However, the application of a relatively low magnetic field effectively suppresses the fast relaxation occurring

through QTM across dimer levels, allowing the observation of slow relaxation within our experimental frequency range. In particular, a positive out-of-phase signal emerges for magnetic fields exceeding 0.2 kOe, although, the relaxation time is not sufficiently slow and the maxima in the χ'' falls at frequencies larger than 10 kHz, even at the lowest temperatures (see Fig 6c,d). Variation with temperature is obtained at an optimum field of 1.2 kOe. Relaxation times are determined through a $\chi'(f)$, $\chi''(f)$ double fit employing a Debye model (see S2). Consistent results are obtained using the Kramers-Kronig relation. The acquired spin relaxation time exhibits an Arrhenius temperature dependence, with τ_0=8(6) x 10^{-8} s and U_{eff}/k_B=10(2) K. It is noteworthy that the estimated energy barrier is likely underestimated, considering the restricted temperature range for measuring this process. Nevertheless, based on the static characterization, the Er_2Ba complex can be effectively modeled as a chain of dimers strongly AF coupled (J'/k_B = -8.6 K). Consequently, the observed dynamics may be ascribed to the single-ion relaxation of Er(III) within the dimer unit. The dominant role in this scenario is played by the energy level splitting at the dimer level, which is of the order of 17 K.

The behaviour of this complex resembles that of its terbium analog, Tb_2Ba,[25] concerning magnetic interactions along the chain and AF dimer formation, although the dimeric interaction is notably stronger for Er_2Ba. The elevated energetic levels of the dimers in this case enhances relaxation through a thermally activated process. Although for an AF coupled dimer the ground state at zero field has a zero spin, and the magnetization would drop to a null value, in the presence of a magnetic field and at higher temperatures the AF coupling is overcome. This leads to the observation of a characteristic slow relaxation of magnetization, attributed to spin polarization, level mixing, and an increased population of excited magnetic states.

Ho_2Ba (3)

The $\tau(1/T)$ and $\tau(H)$ relaxation time dependencies of the very slow process observed for complex **3**, Fig. 6e,f, are characteristic of a direct process affected by phonon-bottleneck (PB) effect, a mechanism that we have commonly encountered in these polymeric furoate complexes[25] and other metal-organic compounds.[44,45] Spin relaxation time is nearly independent of both, magnetic field strength and temperature, resulting

in a constant value of approximately τ = 0.4(1) s. The overall behaviour of **3** is reminiscent of that previously reported in the non-Kramers Tb monomeric[22] and heterometallic[25] furoate compounds. The emergence of a magnetic field-induced temperature-independent relaxation time is attributed to a direct process. The formation of dimers in the chain does not appear to exert a strong influence on the detected spin relaxational behavior.
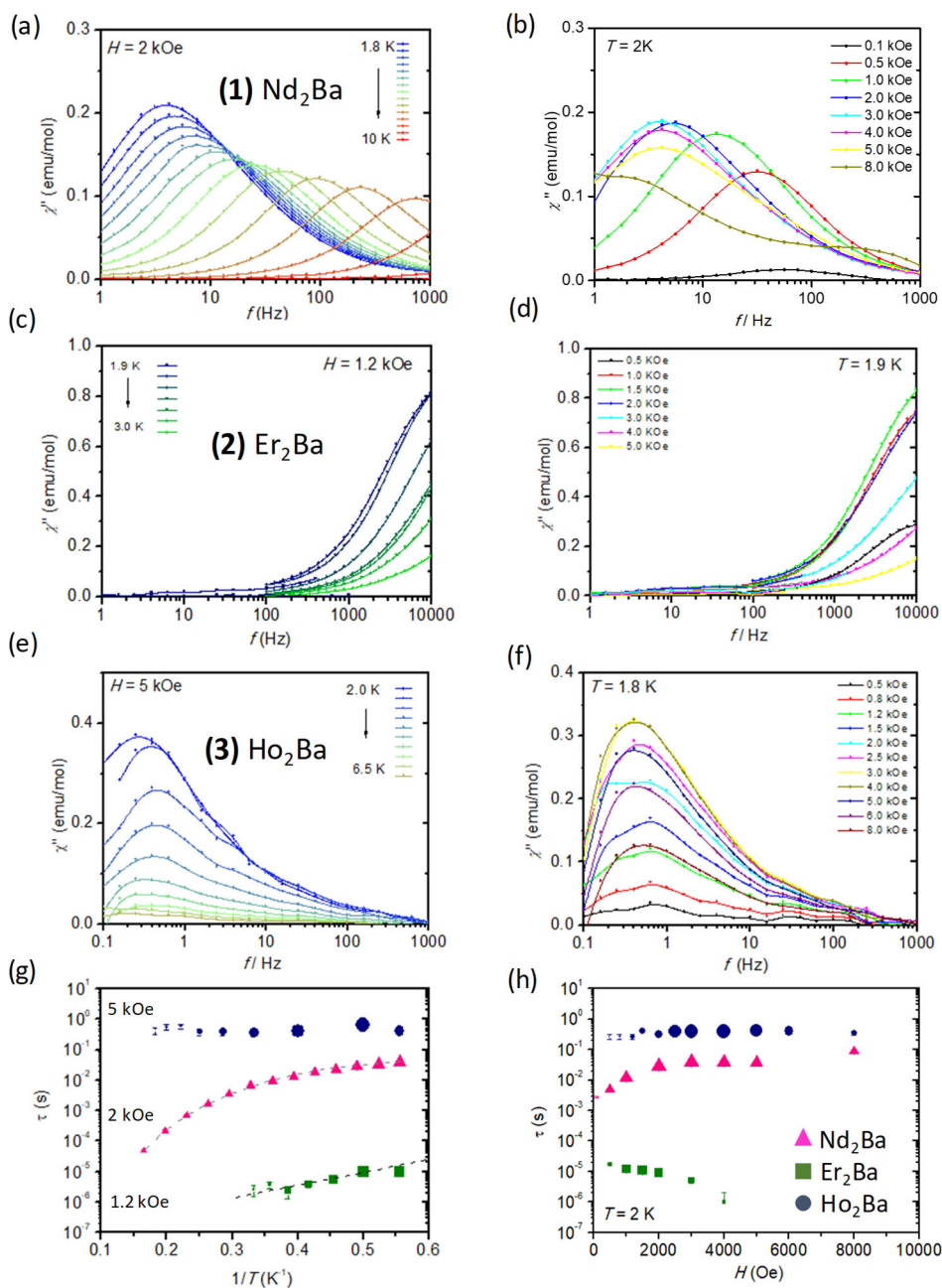
Figure 6. *Imaginary components of the ac susceptibility as a function of frequency, $\chi''(f)$ of complexes **1** (Nd₂Ba), **2** (Er₂Ba) and **3** (Ho₂Ba). Left column: depicts $\chi''(f)$ variation as a function of temperature at constant temperature, 2 K, and Right column: depicts $\chi''(f)$ variation as a function of temperature at constant field. Bottom: relaxation time as a function of (g) the inverse temperature, $\tau(1/T)$, and (h) as a function of the magnetic field, at T=2 K for the three compounds. The size of the symbols is proportional to the intensity of the χ'' peak. Light gray dashed line in (g) is the fit for **1** to Eq. (1), with parameters: τ_{QT}= 0.05(1) s, C = 0.183(4) $s^{-1}K^{-6}$, n=6.0(5), and τ_0= 3.5(5) 10^{-9} s, U_{eff}/k_B=60(1) K. Dark gray dashed line in (g) is the fit for **2** to an Arrhenius law with τ_0= 8(6) 10^{-8} s and U_{eff}/k_B=10(2) K.*

6. Discussion and Conclusions

Table 2 summarizes the results obtained in this study for Ln₂Ba (Ln=Nd, Er, Ho) compounds, in conjunction with previously reported results for dimeric Ln₂Ba (Ln= Dy[24], Tb[25]) and monomeric (Ln=Dy,[20] Tb[22], Nd[21]) members of the family for comparative purposes.

Table 2. *Summary of magnetic properties for all studied lanthanide 1D polymeric nanomagnets of the furoate family.*

Complex (ref.)	EAM angle (chain axis)	Dimer interaction	Intrachain interactions	Interchain interactions Long range order (T_N)	Slow magnetic relaxation mechanisms
(Dy)[20]	50° (DyA) 42° (DyB)	-	FM 0.755 K	-0.135 K (AF) T_N = 0.67 K	TAQT (DyA), U_{eff}=32.4 K TAQT (DyB), U_{eff}=80.5 K Direct (τ_D~1 s)
(Dy₂Ba)[24]	~34°	FM 0.528 K	FM 0.528 K	-0.021 K (AF) T_N = 0.25 K	Orbach (4 kOe), U_{eff}=68 K Direct (τ_D~0.2 s)
(Tb)[22]	~90° (TbA) ~90° (TbB)	-	AF -0.135 K	- No order	SCM (TbA), E_{SCM}=1.0 K SCM (TbB), E_{SCM}=2.0 K Direct (3 kOe), τ_D~1 s
(Tb₂Ba)[25]	~90°	AF -1.6 K	AF -0.15 K	-0.03 K (AF) No order	Orbach 3D, U_{eff}=1.1 K Direct (4.5 kOe), τ_D~1 s
(Nd)[21]	~75°	-	AF -0.255 K	- No order	Orbach (1.2 kOe), U_{eff}=121 K Direct (10 kOe), τ_D~0.1 s
(Nd₂Ba) This work	~40° (Nd1) ~10° (Nd2)	AF -0.08 K	AF -0.08 K	- No order	Orbach (2 kOe), U_{eff}=61 K Direct (8 kOe), τ_D~0.1 s
(Er₂Ba) This work	~90°	AF -8.6 K	AF -0.28 K	- No order	Orbach (1.2 kOe), U_{eff}=10 K
(Ho₂Ba) This work	~90°	AF -2.5 K	AF -	- No order	Direct (5 kOe), τ_D~0.4s

For homometallic, isostructural $\{Ln(\alpha\text{-fur})_3(H_2O)_3\}_n$ compounds, distinct behaviors were observed for Dy (Kramers) and Tb (non-Kramers) analogues. The magnetic structure of (**Dy**)[20] compound was formed by two different types of chains (including either Dy(A) or Dy(B) sites) having ferromagnetic (FM) intrachain coupling (J'/k_B = 0.755 K). The two Dy sites, differing only in the position of one capping ligand, exhibited SIM relaxation through Thermally Activated Quantum Tunneling (TAQT) with distinct activation energies of 80.5 K and 32.4 K, entering a QTM regime upon cooling. As the temperature was decreased, weak interchain AF coupling (J'''/k_B= - 0.135 K), of dipolar origin, led to AF 3D long-range ordering at T_N = 0.66 K. In the case of the non-Kramers compound (**Tb**),[25] similarly the presence of two slightly different coordination sites, Tb(A) and Tb(B), resulted in the existence of two distinct chain types in the crystal. In both types, the EAM of Tb ions was nearly perpendicular to the chain, and the intrachain coupling was AF ($J'/k_B \sim -0.135$ K) in this case. Under H=0, two Arrhenius-like processes were observed with activation energies of 2.03 K and 1 K, associated to SCM relaxation in the two chain types, facilitated by the presence of defects breaking the chain into shorter segments. In such an AF chain, 3D ordering can never be achieved when approaching $T \rightarrow 0$, unlike in (**Dy**). Instead, it was found that for T<0.1 K the SCM mechanism was replaced by individual relaxation of the ions through direct processes.

The Kramers compound (**Nd**)[21] featured polymeric chains along the a-direction, resembling but not being isostructural to (**Dy**) and (**Tb**), and all Nd sites were equivalent. The EAM was nearly perpendicular to the chain, favoring intrachain AF interactions (J'/k_B= - 0.255 K). The application of a small field of about 80 Oe was sufficient to quench QTM allowing relaxation through slower paths. An activation energy of U_{eff}/k_B=121 K under 1.3 kOe was observed, ranking among the highest reported for Nd single-molecule magnets (SMMs).

Concerning the isostructural dimeric compounds (**Dy₂Ba**)[24] and (**Tb₂Ba**)[25], both featuring 1D zig-zag chains along the c-axis formed by two Ln(III), with identical coordination environment, separated by Ba ions, their relaxational behavior differed significantly. In (**Dy₂Ba**) complex,[24] the EAM of the Dy ions was slightly canted with respect to the c-axis chain direction (34°), resulting in FM intrachain interactions. Intradimer and interdimer interactions were of the same order ($J'/k_B = J''/k_B$= 0.528 K).

The behavior of (**Dy₂Ba**) when approaching T=0 closely resembled that of (**Dy**)[20]: under H=0, relaxation occurs through QTM of the Dy ions until, at T_N = 0.25 K, a long-range 3D ordering state emerges, enabled by the AF interchain coupling (J'''/k_B = - 0.021 K).[24] The application of a magnetic field opened the path for slow relaxation of the Dy ions through an Orbach process (U_{eff}/k_B = 68 K at H=2 kOe), and a second, slower direct process (τ~0.2 s). Conversely, in (**Tb₂Ba**) the EAM was found to be nearly perpendicular to the chain, leading to AF intrachain coupling. The Tb-Tb intradimer AF interaction was significant (J'/k_B = -1.6 K), of the order of the anisotropy energy, while the interdimer interaction was an order of magnitude smaller (J''/k_B = -0.15 K). The dynamical behavior of (**Tb₂Ba**) qualitatively resembled that of (**Tb**). Under H=0, the slow relaxation was assigned to 3D sluggish relaxation of the remaining magnetic moments, possibly enhanced by the presence of defects in the dimeric chain. The observed activation energy (U_{eff}/k_B=1.1 K) in (**Tb₂Ba**) was similar to that of (**Tb**). Under the application of a magnetic field (**Tb₂Ba**), like (**Tb**), exhibited bottlenecked slow relaxation processes.

The new Kramers compound (**Nd₂Ba**) features zig-zag chains along the *a*-axis, like (**Nd**), but in this case the two Nd ions in the dimeric unit have different coordination environment; the EAM of Nd1 is transversal to the chain and close to perpendicular to Nd2, leading to AF interaction. Magnetic dimerization does not play a significant role, and thus the magnetic behavior can be modeled with an average, weak AF intrachain constant, J'/k_B = J''/k_B = -0.08 K. The relaxational behavior of (**Nd₂Ba**) resembles that of (**Nd**), exhibiting field-induced Orbach process with a U_{eff}/k_B =61 K (2 kOe) smaller than in the latter, and a direct process.

In contrast, in the Kramers compound (**Er₂Ba**), isostructural to (**Nd₂Ba**), magnetic dimerization is important: the EAM of the two Er ions, antiparallel to each other, lie close to perpendicular to the chain *c*-axis, and AF intradimer interaction (J'/k_B = −8.6 K) is much larger than interdimer coupling (J''/k_B = −0.28 K). This compounds exhibits a rapid field-induced Orbach-like process, with τ_0= 8(6) x 10⁻⁸ s and U_{eff}/k_B=10 K at kOe.

Finally, the magnetic behavior of non-Kramers compound (**Ho₂Ba**), qualitatively resembles that of isostructural (**Tb₂Ba**) and can be explained by a highly anisotropic quasi-doublet with a Δ_{Ho}/k_B = 0.7 K gap. Non-Kramers Ho ions form magnetic dimers

within the Ho_2Ba cluster, coupled by an AF intradimer interaction $J'/k_B = -2.5$ K, and slow relaxation is only observed through a direct process.

In conclusion, the systematic exploration of the α-furoate family of lanthanide polymeric chains unveils a diverse phenomenology in magnetization relaxation behavior, highlighting the intricate interplay among specific ions, magnetic anisotropy, and the relative strength and sign of interactions.

Acknowledgements

References

1   D. Shao and X.-Y. Wang, *Chin. J. Chem.*, 2020, **38**, 1005－1018.
2   A. Gaita-Ariño, F. Luis, S. Hill and E. Coronado, *Nat Chem*, 2019, **11**, 301 – 309.
3   R. A. Layfield and M. Murugesu, *Lanthanides and Actinides in Molecular Magnetism*, Wiley-VCH Verlag&Co. KGaA, 2015.
4   E. Bartolomé, A. Arauzo, J. Luzón, J. Bartolomé and F. Bartolomé, in *Handbook of Magnetic Materials*, 2017, vol. 26, pp. 1–289.
5   J. Rinehart and J. Long, *Chem. Sci.*, 2011, **2**, 2078–2085.
6   M. A. Sørensen, U. B. Hansen, M. Perfetti, K. S. Pedersen, E. Bartolomé, G. G. Simeoni, H. Mutka, S. Rols, M. Jeong, I. Zivkovic, M. Retuerto, A. Arauzo, J. Bartolomé, S. Piligkos, H. Weihe, L. H. Doerre and J. Bendix, *Nat Commun*, 2018, **9**, 1292.
7   K. S. Pedersen, L. Ungur, M. Sigrist, A. Sundt, M. Schau-Magnussen, V. Vieru, H. Mutka, S. Rols, H. Weihe, O. Waldmann, L. F. Chibotaru, J. Bendix and J. Dreiser, *Chem Sci*, 2014, **5**, 1650–1660.
8   Y. S. Ding, K. X. Yu, D. Reta, F. Ortu, R. E. P. Winpenny, Y. Z. Zheng and N. F. Chilton, *Nat Commun*, 2018, **9**, 3134.
9   F. S. Guo, B. M. Day, Y. C. Chen, M. L. Tong, A. Mansikkamäki and R. A. Layfield, *Science*, 2018, **364**, 1400–1403.
10   C. Wäckerlin, F. Donati, A. Singha, R. Baltic, S. Rusponi, K. Diller, F. Patthey, M. Pivetta, Y. Lan, S. Klyatskaya, M. Ruben, H. Brune and J. Dreiser, *Advanced Materials*, 2016, **28**, 5195–5199.
11   T. Morita, M. Damjanović, K. Katoh, Y. Kitagawa, N. Yasuda, Y. Lan, W. Wernsdorfer, B. K. Breedlove, M. Enders and M. Yamashita, *J Am Chem Soc*, 2018, **140**, 2995–3007.
12   F. Luis, A. Repollés, M. J. Martínez-Pérez, D. Aguilá, O. Roubeau, D. Zueco, P. J. Alonso, M. Evangelisti, A. Camón, J. Sesé, L. A. Barrios and G. Aromí, *Phys Rev Lett*, 2011, **107**, 117203–117208.

13   E. Moreno-Pineda, S. Klyatskaya, P. Du, Damjanovic, G. Taran, W. Wernsdorfer and M. Ruben, *Inorg Chem*, 2018, **57**, 9873–9879.

14   E. Bartolomé, J. Bartolomé, A. Arauzo, J. Luzón, R. Cases, S. Fuertes, V. Sicilia, A. I. Sánchez-Cano, J. Aporta, S. Melnic, D. Prodius and S. Shova, *J Mater Chem C Mater*, 2018, **6**, 5286–5299.

15   W. X. Zhang, R. Ishikawa, B. Breedlove and M. Yamashita, *RSC Adv*, 2013, **3**, 3772–3798.

16   F. C. Liu, Y. F. Zeng, J. P. Zhao, B. W. Hu, X. Hu, J. Ribas and X. H. Bu, *Dalton Transactions*, 2009, 2074–2076.

17   M. Ahmad Yatoo, G. Cosquer, M. Morimoto, M. Irie, B. K. Breedlove, M. Yamashita, M. Andruh and L. F. Chibotaru, *Magnetochemistry 2016, Vol. 2, Page 21*, 2016, **2**, 21.

18   A. B. Ruiz-Muelle, A. García-García, A. A. García-Valdivia, I. Oyarzabal, J. Cepeda, J. M. Seco, E. Colacio, A. Rodríguez-Diéguez and I. Fernández, *Dalton Transactions*, 2018, **47**, 12783–12794.

19   A. Arauzo, A. Lazarescu, S. Shova, E. Bartolomé, R. Cases, J. Luzón, J. Bartolomé and C. Turta, *Dalton Trans*, 2014, **43**, 12342–12356.

20   E. Bartolomé, J. Bartolomé, S. Melnic, D. Prodius, S. Shova, A. Arauzo, J. Luzón, F. Luis and C. Turta, *Dalton Transactions*, 2013, **42**, 10153–10171.

21   E. Bartolomé, A. Arauzo, J. Luzón, S. Melnic, S. Shova, D. Prodius, I. C. Nlebedim, F. Bartolomé and J. Bartolomé, *Dalton Transactions*, 2019, **48**, 15386–15396.

22   E. Bartolomé, J. Bartolomé, A. Arauzo, J. Luzón, L. Badía, R. Cases, F. Luis, S. Melnic, D. Prodius, S. Shova and C. Turta, *J. Mater. Chem. C*, 2016, **4**, 5038–5050.

23   E. Bartolomé, J. Bartolomé, A. Arauzo, J. Luzón, R. Cases, S. Fuertes, V. Sicilia, A. I. Sánchez-Cano, J. Aporta, S. Melnic, D. Prodius and S. Shova, *J Mater Chem C Mater*, 2018, **6**, 5286–5299.

24   E. Bartolomé, J. Bartolomé, S. Melnic, D. Prodius, S. Shova, A. Arauzo, J. Luzón, L. Badía-Romano, F. Luis and C. Turta, *Dalton Trans*, 2014, **43**, 10999–1013.

25   E. Bartolomé, A. Arauzo, J. Luzón, S. Melnic, S. Shova, D. Prodius, J. Bartolomé, A. Amann, M. Nallaiyan and S. Spagna, *Dalton Transactions*, 2019, **48**, 5022–5034.

26   Y. Chen, R. Gao, X. Zhao, Z. Ruan, J. Lin, Z. tian and S. Liu, *J Mol Struct*, 2021, **1224**, 129301.

27   Y. Chen, X. Zhao, R. Gao, Z. Ruan, J. Lin, S. Liu, Z. Tian and X. Chen, *J Solid State Chem*, 2020, **292**, 121674.

28   M. A. Shmelev, R. A. Polunin, N. V. Gogoleva, I. S. Evstifeev, P. N. Vasilyev, A. A. Dmitriev, E. A. Varaksina, N. N. Efimov, I. V. Taydakov, A. A. Sidorov, M. A. Kiskin, N. P. Gritsan, S. V. Kolotilov and I. L. Eremenko, *Molecules 2021, Vol. 26, Page 4296*, 2021, **26**, 4296.

29   Y. Chen, W. Chen, Z. Ju, Q. Gao, T. Lei, W. Liu, Y. Li, D. Gao and W. Li, *Dalton Transactions*, 2013, **42**, 10495–10502.

30   Y. Chen, Q. Gao, D. Gao, D. Wang, Y. Li, W. Liu and W. Li, *J Coord Chem*, 2013, **66**, 3829–3838.

31   J. Hou, Y. Chen, L. Zhu, S. Zou and W. Dong, *Polyhedron*, 2022, **220**, 115836.

32   S. Melnic, D. Prodius, S. Shova, H. Stoeckli-Evans, Y. Simonov, A. Feher, M. Gdaniec and C. Turta, *Chem. J. Moldova*, 2009, **4**, 60.

33   J. A. F. Aquilante, R. K. Carlson, L. F. Chibotaru, M. G. Delcey, L. De Vico, I. Fdez. Galván, N. Ferré, L. M. Frutos, L. Gagliardi, M. Garavelli, A. Giussani, C. E. Hoyer, G. L. Manni, H. Lischka, D. Mamá, P. Å. Malmqvist, T. Müller, A. Nenov, M. Olivucci, P. T. B, D. Peng, F. Plasser, B. Pritchard, M. Reiher, I. Rivalta, I. Schapiro, J. Segarra-Martí, M. Stenrup and Michael, *J. Comp. Chem.*, 2016, **37**, 506–541.

34   G. Cucinotta, M. Perfetti, J. Luzon, M. Etienne, P. E. Car, A. Caneschi, G. Calvez, K. Bernot and R. Sessoli, *Angewandte Chemie - International Edition*, 2012, **51**, 1606–1610.

35   *Rigaku Oxford Diffraction, CrysAlisPro Software system (2015).*, 2015.

36   G. M. Sheldrick, *Acta Crystallogr A*, 2015, **71**, 3–8.

37   G. M. Sheldrick, *Acta Crystallogr C Struct Chem*, 2015, **71**, 3–8.

38   O. V. Dolomanov, L. J. Bourhis, R. J. Gildea, J. A. K. Howard and H. Puschmann, *J Appl Crystallogr*, 2009, **42**, 339–341.

39   S. Melnic, D. Prodius, S. Shova, H. Stoeckli-Evans, Y. Simonov, A. Feher, M. Gdaniec and C. Turta, *Chem. J. Mold.*, 2009, **4**, 61–69.

40   D. Aguilà, L. A. Barrios, V. Velasco, O. Roubeau, A. Repollés, P. J. Alonso, J. Sesé, S. J. Teat, F. Luis and G. Aromí, *J Am Chem Soc*, 2014, **136**, 14215–14222.

41   K. S. Chilton, N. F.; Anderson, R. P.; Turner, L. D.; Soncini, A.; Murray, *J. Comput. Chem.*, 2013, **34**, 1164–1175.

42   H. Van Kempen, A. R. Miedema and W. J. Huiskamp, *Physica*, 1964, **30**, 229–236.

43   A. Abragam and B. Bleaney, in *Electron Paramagnetic Resonance of Transition Ions*, Clarendon Press - Oxford, 1970, p. Chapter 10.

44   A. Arauzo, E. Bartolomé, A. C. Benniston, S. Melnic, S. Shova, J. Luzón, P. J. Alonso, A. L. Barra and J. Bartolomé, *Dalton Transactions*, 2017, **46**, 720–732.

45   J. González, P. Sevilla, G. Gabarró-Riera, J. Jover, J. Echeverría, S. Fuertes, A. Arauzo, E. Bartolomé and E. C. Sañudo, *Angewandte Chemie - International Edition*, 2021, **60**, 12001–12006.

Supplementary Information

Low temperature magnetism of Ln₂Ba (Ln=Nd, Er, Ho) furoate-based polymeric chains: slow relaxation, magnetic anisotropy and interactions

Ana Arauzo,[a*] Elena Bartolomé,[b,c*] Javier Luzón,[a,d] Silvia Melnic,[e,f] Sergiu Shova[g] and Juan Bartolomé[a]

[a]Instituto de Nanociencia y Materiales de Aragón (INMA), CSIC-Universidad de Zaragoza, Pedro Cerbuna 12,50009 Zaragoza, Spain. E-mail: aarauzo@unizar.es
[b]Institut de Ciència de Materials de Barcelona (ICMAB), Bellaterra, Spain, E-mail: ebartolome@icmab.es
[c]Escola Universitària Salesiana de Sarrià (EUSS), Passeig Sant Joan Bosco 74, 08017-Barcelona, Spain. E-mail: ebartolome@euss.es
[d]Centro Universitario de la Defensa, Academia General Militar, Zaragoza, Spain
[e]Moldova State University, Institute of Chemistry, Academiei 3, MD-2028 Chisinau, Republic of Moldova
[f]"Nicolae Testemitanu" State University of Medicine and Pharmacy, bd. Stefan cel Mare şi Sfant 165, MD-2004 Chisinau, Republic of Moldova
[g]"Petru Poni" Institute of Macromolecular Chemistry, Alea Gr. Ghica Voda 41A, 700487 Iasi, Romania
(*) E-mail: aarauzo@unizar.es; ebartolome@icmab.es

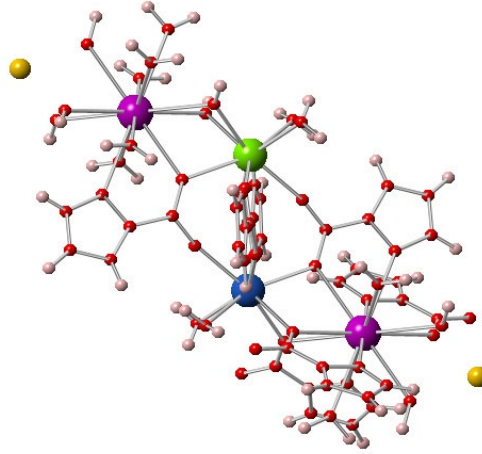## S1. *Ab initio* model cluster

Figure S1. *Model cluster employed for ab initio simulations. Color code: Ln(III) ion (Ln=Nd (1), Er (2), Ho (3)) (blue), La (green), Ba (purple), C (red), H (grey), point charges, +1 (yellow).*

S2. Ac Magnetic susceptibility.

Debye Model.

Equations for ac magnetic susceptibility. For a single relaxation process with time τ.

$$\chi*(\omega) = \chi' + i\chi'' = \chi_\infty + \frac{(\chi_0 - \chi_\infty)}{1 + i\omega\tau}$$

$$\chi' = \chi_\infty + \frac{(\chi_0 - \chi_\infty)}{1 + \omega^2\tau^2} \qquad \chi'' = \frac{(\chi_0 - \chi_\infty)\omega\tau}{1 + \omega^2\tau^2}$$

For a distribution of relaxation times, given by the parameter α (0 for a single relaxation time).

$$\chi*(\omega) = \chi' + i\chi'' = \chi_\infty + \frac{(\chi_0 - \chi_\infty)}{1 + (i\omega\tau)^{(1-\alpha)}}$$

Measurement window

$0.1 \leq f \leq 10^4$ Hz $\quad \rightarrow \quad 1.6 \ 10^{-5}$ s $\leq \tau \leq 1.6$ s

Expanded window by double fitting of χ' and χ" to the Debye Model, or by using the Kramers-Kronig relation:

$$\tau = \frac{\chi''}{(\chi' - \chi_\infty)\omega}$$
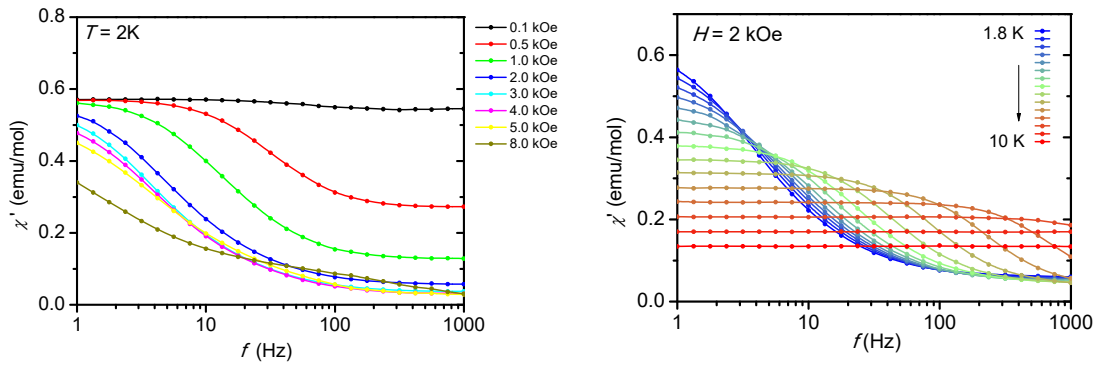
Additional Figures

Nd₂Ba (1)

Figure S2. *In-phase magnetic susceptibility, χ'(f) for different magnetic fields (left) and temperatures (right) for Nd₂Ba.*
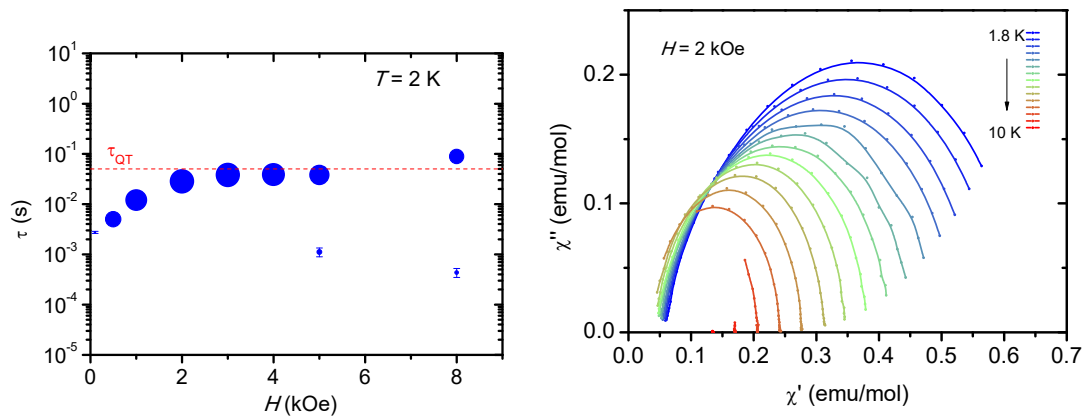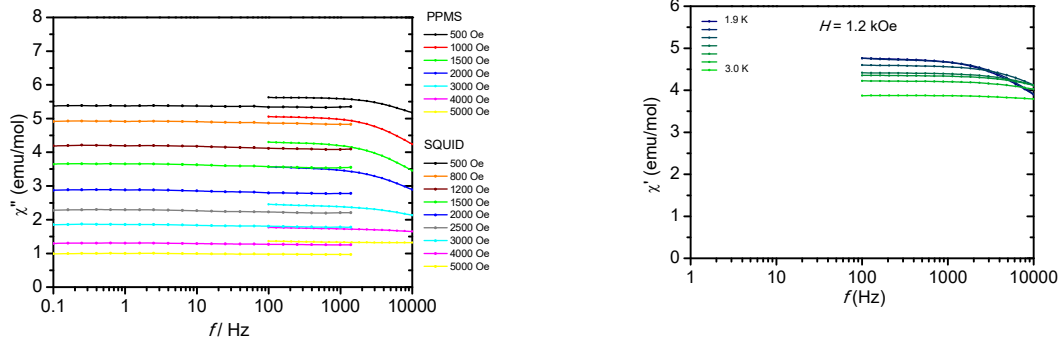

Figure S3. *Left: Relaxation time at T = 2 K as a function of magnetic field τ(H). Red dashed line shows the quantum tunneling relaxation time, τ_{QT} obtained from the τ(T⁻¹). fit (see main text) for compound 1 (Nd₂Ba). Right. χ"(χ') Cole-Cole plot for 1.*

Er₂Ba (2)

Figure S4. *In-phase magnetic susceptibility, χ'(f) for different magnetic fields (left) and temperatures (right) for Er₂Ba.*
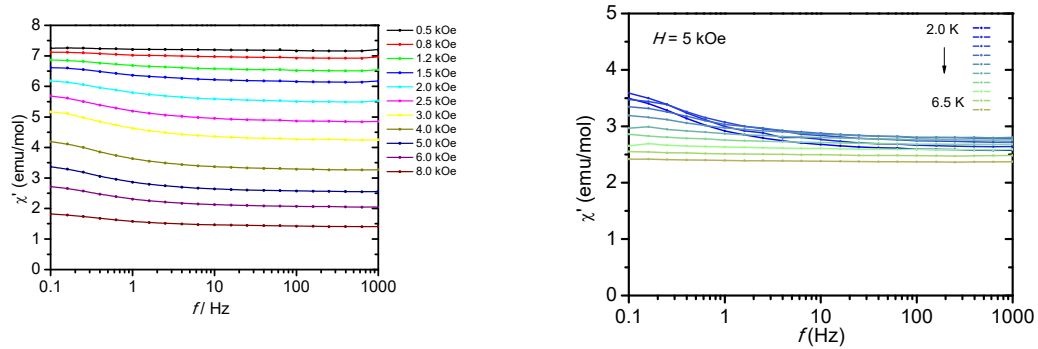
Ho₂Ba (3)

Figure S5. *In-phase magnetic susceptibility, χ'(f) for different magnetic fields (left) and temperatures (right) for Ho₂Ba.*